Journal of Nuclear Medicine, published on October 20, 2016 as doi:10.2967/jnumed.116.174508

# Modeling strategies for quantification of in vivo $^{18}$F-AV1451 binding in patients with tau pathology

Andreas Hahn[1#], Martin Schain[2], Maria Erlandsson[3],
Petter Sjölin[3], Gregory M James[1], Olof T Strandberg[2], Douglas Hägerström[4],
Rupert Lanzenberger[1], Jonas Jögi[5], Tomas G Olsson[3], Ruben Smith[6*], Oskar Hansson[2,7*#]

*[1] Department of Psychiatry and Psychotherapy, Medical University of Vienna, Austria*
*[2] Clinical Memory Research Unit, Department of Clinical Sciences, Malmö, Lund University, Sweden*
*[3] Department of Radiation Physics, Skåne University Hospital, Lund, Sweden*
*[4] Department of Clinical Neurophysiology, Skåne University Hospital, Lund, Sweden*
*[5] Department of Clinical Physiology and Nuclear Medicine, Skåne University Hospital, Lund, Sweden*
*[6] Department of Neurology, Skåne University Hospital, Lund, Sweden*
*[7] Memory Clinic, Skåne University Hospital, Malmö, Sweden*

For revision in the **Journal of Nuclear Medicine**

| Word count | 342 | Abstract |
|---|---|---|
| | 2769 | Main section |
| Tables: 2, Figures: 6, References: 28, Supplement: 12 pages | | |

**Keywords:** Tau imaging, positron emission tomography, kinetic modeling, quantification
**Running title:** Tau quantification with $^{18}$F-AV1451

*** Equal contribution as senior authors**

**[#] Correspondence to:** Andreas Hahn, Ass.Prof.
Department of Psychiatry and Psychotherapy
Medical University of Vienna, Austria
Waehringer Guertel 18-20, 1090 Vienna, Austria
Email: andreas.hahn@meduniwien.ac.at

or

Oskar Hansson, Assoc.Prof. MD
Memory Clinic, Skåne University Hospital
SE-20502 Malmö, Sweden
E-mail: oskar.hansson@med.lu.se

**ABSTRACT**

Aggregation of hyperphosphorylated tau is a major hallmark of many neurodegenerative diseases, including Alzheimer's disease. *In vivo* imaging with positron emission tomography (PET) may offer important insights in pathophysiological mechanisms, diagnosis and disease progression. We describe different strategies for quantification of $^{18}$F-AV1451 (T807) tau binding, including models with blood sampling and non-invasive alternatives.

**Methods:** 15 subjects (4 controls, 6 Alzheimer's disease (AD), 3 progressive supranuclear palsy (PSP), 2 cortico basal syndrome (CBS)) underwent 180 min PET with $^{18}$F-AV1451 and arterial blood sampling. Modeling with arterial input functions included one-, two- and three-tissue compartment models and the Logan plot. Using cerebellum as reference region, the simplified reference tissue model 2 and Logan reference plot were applied. Finally, simplified outcome measures were calculated as ratio with reference to cerebellum concentrations *(SUVR)* and standard uptake values.

**Results:** Tissue compartment models were not able to describe the kinetics of $^{18}$F-AV1451 with poor fits in 33-53% of cortical regions and 80% in subcortical areas. In contrast, Logan plot showed excellent fits and parameter variance ($V_T$ standard error < 5%). Compared to the 180 min arterial-based Logan model, strong agreement was obtained for the Logan reference plot also for reduced scan time of 100 min ($R^2$ = 0.91) and *SUVR* 100-120 min ($R^2$ = 0.94), with 80-100min already representing a reasonable compromise between duration and accuracy ($R^2$ = 0.93). Time activity curves and kinetic parameters were equal for cortical regions and the cerebellum in control subjects, but different in the putamen. Cerebellar total volumes of distribution were higher in controls than patients. For the above methods, increased cortical binding was observed for AD patients and to some extent for CBS, but not PSP.

**Conclusions:** Using arterial input functions, the Logan plot provided the best estimate of tau binding. Assuming that cerebellum is a valid reference region, simplified methods seem to provide robust alternatives for quantification, such as the Logan reference plot with 100 min scan time. Furthermore, *SUVR* ratios between target and cerebellar activities obtained from a 80-100 min static scan offer promising potential for clinical routine application.

## INTRODUCTION

Alzheimer's disease is a neurodegenerative disorder with progressing dementia, neuropathologically characterized by amyloid-beta deposition in the form of senile plaques and aggregation of hyperphosphorylated tau as neurofibrillary tangles, leading to neuronal dysfunction and cell death (*1, 2*). The formation of amyloid-beta plaques may already occur even decades before symptom onset, whereas tau deposition is more closely related to the disease duration and severity (*3, 4*), making it a potentially important marker for monitoring disease progression and treatment strategies (*5*). Furthermore, tau aggregation is implicated in a series of other neurodegenerative diseases such as cortico basal syndrome, progressive supranuclear palsy and frontotemporal dementia.

Although biomarkers obtained from cerebrospinal fluid demonstrate great clinical utility (*6*), the procedure does not yield information about the spatial distribution of tau pathology in the brain. Hence, robust non-invasive imaging markers would offer an important advancement for diagnosis and monitoring of disease progression. Several PET radioligands have been developed with high sensitivity for tau (*1, 7*) (supplement). Among those, $^{18}$F-AV1451 shows promising characteristics for tau quantification. The radioligand exhibits a more than 25-fold higher sensitivity for tau than amyloid beta (*8*), a high gray to white matter contrast (*9*) and negligible non-specific binding to several other targets such as monoamine oxidase A and B (*8*). Further, radioactive metabolites of $^{18}$F-AV1451 are unlikely to pass the blood brain barrier (*8*) and little tracer uptake in the bone has been reported (*9*). Initial human studies have demonstrated increased binding in patients with AD and mild cognitive impairment when compared to healthy controls (*10*). Although quantification with reference region models and ratio methods was recently reported (*11*), validation with arterial blood sampling and scan durations > 100 min is still missing.

The aim of this work was to establish an optimal quantification procedure for tau binding with $^{18}$F-AV1451, both for research related and clinical purposes. This included the identification of an optimal modeling strategy with arterial blood sampling as gold standard, the assessment of non-invasive alternatives and simplified ratio methods. We further evaluated different scan time intervals between 40 and 180 min when using standard uptake values (SUV) and ratios (*SUVR*) for potential clinical applicability when separating AD patients from controls.

## METHODS

### Subjects

Fifteen subjects participated in this study. These included 4 healthy controls (HC, mean age±sd = 75.0±3.8 years, 1 female), 6 patients with Alzheimer's disease (AD, 64.8±14.7 years, 2 female), 2 patients with cortico basal syndrome (CBS, 66.5±0.7 years, 2 females) and 3 patients with progressive supranuclear palsy (PSP, 74.3±5.8 years, 0 females). See supplement for clinical evaluation and exclusion criteria. All subjects signed a written informed consent after detailed explanation of the study protocol. The procedures were approved by the Ethical Review Board of Lund University (2014-233) and the Swedish Medical Products Agency. All procedures were carried out according to the Declaration of Helsinki.

### Positron emission tomography

Subjects underwent a 180min PET examination with $^{18}$F-AV1451 on a GE Discovery 690 PET/CT (General Electric Medical Systems, Milwaukee, WI, USA) scanner at Skåne University Hospital, Lund, Sweden. See supplement for radiolabeling and acquisition details. Mean i.v. injected dose was 371.1±14.1 MBq (5.58±1.43 MBq/kg body weight) and the radioligand was administered as a bolus over 40s.

### Blood sampling

A cannula was inserted into the radial artery, after which arterial blood samples were obtained manually (supplement). Radioactive metabolites were determined using high performance liquid chromatography (supplement). The parent fraction was fitted with a Hill function (*12*), multiplied with the plasma curve which was finally fitted with a tri-exponential function from the peak onwards to obtain the arterial input function. The individual delay of the radioligand between the sampling site (A. radialis) and the brain was estimated by modeling a whole-brain time activity curve (*13*).

**Data processing**

Coregistration, spatial normalization and segmentation were performed with the Advanced Neuroimaging Tools (ANT, http://stnava.github.io/ANTs/, supplement).

**Regions of interest**

Regions of interest were derived from the Harvard-Oxford atlas and the probabilistic cerebellar atlas provided in FSL (http://fsl.fmrib.ox.ac.uk/fsl/). These were frontal, temporal, parietal, occipital and cingulate cortices, thalamus, putamen, caudate, hippocampus and the cerebellar gray matter excluding vermis (and hence also excluding the dentate nucleus, potentially showing increased binding in PSP patients, supplement).

**Quantitative analysis**

To estimate tau binding several quantification strategies were employed (Table 1). The optimal model was identified based on the structure of residuals (*14*), goodness of fit (Akaike information criterion) and variance of the outcome parameter (% standard error, Marquart-Levenberg optimization calculated in PMOD). Using the arterial input function, we applied one-, two- or three-tissue compartment models (TCM) with and without $K_1/k_2$ coupled across regions as well as the Logan plot (*15*). The primary outcome parameter was the total volume of

distribution ($V_T$) for 1TCM and Logan plot as well as the specific volume of distribution or binding potential ($V_S = BP_P$) for 2TCM and 3TCM (*16*). Assuming that the cerebellum contains only non-displaceable binding (discussion and (*17*)), we also computed $V_S = V_T - V_{T\_cerebellum}$, the distribution volume ratio $DVR = V_T / V_{T\_cerebellum}$ and $BP_{ND} = (V_T - V_{T\_cerebellum}) / V_{T\_cerebellum}$ from the Logan plot. These metrics served for comparison with simplified methods (Table 2). The cerebral blood volume component was fixed to 5% for all models and brain regions.

Reference region models were applied including the simplified reference tissue model 2 (SRTM2) (*18*) and the Logan reference plot (*19*), with the cerebellum as reference, yielding $BP_{ND}$ and $DVR = BP_{ND} + 1$ *as* outcome measure, respectively. For the Logan reference plot, $k_2'$ was estimated with the SRTM2 in temporal and cerebellar cortices. For direct comparison, the calculations with the SRTM2 were additionally carried out with the same $k_2'$ fixed for all regions. Shortened scan time was evaluated for the Logan reference plot for 60, 100 and 140min. Finally, ratio methods were evaluated for simplified application in clinical routine. These included the ratio between the activity in the target region and the activity in the cerebellum $SUVR = C_{target} / C_{cerebellum}$. Standard uptake values (SUV) were calculated as the activity in the target region divided by the injected dose per kg body weight. For the ratio methods and SUV, the activities were averaged for following intervals: 40-60, 80-100, 120-140 and 160-180 min post injection plus 100-120, 80-110, 90-120, 100-130 and 110-140 min for *SUVR*. All modeling procedures were carried out in PMOD 3.703 (PMOD Technologies, Zurich, Switzerland, www.pmod.com).

**Statistics**

To assess the similarity between the optimal 180 min arterial-based model and simplified methods (reference region models, ratio methods and SUV with shortened scan time), linear regression analysis was computed across all brain regions and subjects. Here, outcome parameters from simplified methods were compared with the correspondingly transformed

outcome from the arterial-based Logan plot; e.g., *SUVR* compared to $DVR = V_T/V_{T\_Cereb}$ from arterial-based Logan plot, etc (Table 2). This yields $R^2$ as a value of reproducibility as well as slope and intercept indicating constant bias and scaling errors, respectively. For clinical applicability, the difference between AD patients and controls was calculated using independent samples t-tests, in order to normalize for differences in the variance for different outcome measures. Due to the low sample size this comparison was not carried out for CBS and PSP patients.

## RESULTS

### Blood data

Whole blood and plasma activities showed rapid clearance of the radioligand from plasma (Fig. 1a). Plasma-to-whole blood ratios approached 1 after 20 min and increased slowly throughout the measurement (Fig. 1b). Metabolism occurred at a moderate pace, with approximately 50% parent compound being available after 30 min (Fig. 1b). In line with previous studies (*8, 20*), a single radioactive metabolite was observed with high performance liquid chromatography (presumably $^{18}F^-$), which was more polar than the parent compound (retention times, 3.7 and 7.5min, Figs. 1c and 1d) and was thus considered unlikely to pass the blood brain barrier.

### Arterial-based models

The delay of the input function was -0.8±2.9 s (range = -6.7…3.4 s). None of the compartment models adequately described the data for all subjects or regions (Fig. 2, Supplemental Figs. 1 and 3). In contrast, the Logan plot showed excellent fits (Fig. 2c) and parameter variance (all $V_T$ < 5% error, Supplemental Fig. 2c) with start of the linear part at t* = 26.1±17.8min. Therefore, the Logan plot was used as the standard for comparison with the simplified analyses.

**Reference region models**

The SRTM2 showed higher parameter variance for $BP_{ND}$ (51.3±131.0% error) as compared to the Logan reference plot *DVR* (0.5±0.4 % error). Still, both methods yielded excellent agreement with the respective outcome measure obtained from arterial-based Logan plot ($R^2$ = 0.92 and 0.99, respectively) and little bias (Table 2). Shortened scan time lowered the association with the arterial-based Logan plot and increased bias. Good agreement was observed until 100 min ($R^2$ = 0.91), but for 60 min $k_2'$ could not be estimated reliably for 2 subjects (1 HC, 1 PSP).

**Ratio methods**

*SUVR* showed strong agreement with the arterial-based Logan plot ($R^2$ = 0.88-0.94, Table 2). Although *SUVR* correlations were similar for all intervals > 80 min, 100-120 min performed best, whereas 80-100 min may represent a reasonable compromise between duration and accuracy. For SUV, only moderate agreement with the arterial-based Logan $V_T$ was obtained ($R^2$ = 0.69-0.82) with highest correlations occurring for 120-140 min. Figure 3 shows time activity curves normalized by injected dose (SUV), by plasma activity and by the cerebellum (*SUVR*). Interestingly, the putamen showed rather different kinetics than any other brain region, especially for healthy controls.

**Group differences in $^{18}$F-AV1451 binding**

Compared to cerebellum, average binding in HC was similar for cortical regions and the hippocampus, but higher for subcortical areas. Logan $V_T$ was markedly higher for AD patients than HC across all cortical regions, whereas for PSP and CBS patients Logan $V_T$ was slightly lower for all regions (Fig. 4a). Conversely, Logan $V_T$ in the cerebellum was lower in all patient groups when compared to HC (16.5%). This seems to be attributable to a minor extent to

differences in gray matter volume, which was 8.1% lower in patients. Correcting for the differences in cerebellar $V_T$, Logan $V_S$ showed more pronounced differences between AD and HC including the hippocampus and slightly increased binding for CBS patients in temporal, parietal and occipital cortices (Fig. 4b). Similarly, *SUVR* calculated for 80-100 min, resulted in 1.6 to 2.2-fold higher binding for AD and up to 1.3-fold increased binding for CBS in the cortex (Fig. 4c). Differences between PSP and HC were generally low for Logan $V_S$ and *SUVR*.

Assessing group differences between AD patients and HC in cortical regions showed best separation for Logan $V_S$ and *SUVR* 80-100 min (Fig. 5). The SRTM2 and Logan reference region models performed almost equally well, whereas SUV methods only yielded differences for selected brain regions.

Voxel-wise quantification confirmed increased binding in AD for Logan plot $V_T$ as well as Logan reference plot *DVR* and *SUVR*, but only to a lesser extent for SUV (Fig. 6).

## DISCUSSION

We evaluated various strategies for quantification of tau binding with the radioligand $^{18}$F-AV1451. Tissue compartment models did not describe the kinetics appropriately, whereas the Logan plot yielded excellent fits and low parameter variance. Reference region models as well as *SUVR* gave strong agreement with the Logan plot.

We observed that none of the compartment models were able to describe the kinetics of $^{18}$F-AV1451 with 33-53% modeling failures in cortex and 80% in subcortical regions. Still, it is possible that more complex compartmental configurations may yield better fits, however, such approaches often come at the expense of increased parameter variance. Although no indications were found that parameter coupling alone or metabolites would explain the lack of compartment model fits, future studies are required to clarify this issue. We propose binding estimates from the Logan plot as the currently best arterial-based solution. In line, usage of

graphical analyses has been suggested for the quantification of $^{11}$C-PBB3 tau binding (*21*) and $^{11}$C-PiB amyloid binding (*22*). For $^{11}$C-PBB3, the lack of adequate fits with compartment modeling may be ascribed to radiometabolites entering the brain (*21*). Conversely, good 2TCM fits were obtained for (S)-$^{18}$F-THK5117 but the corresponding outcome parameters could not be robustly identified, hence, simplified methods were also evaluated with reference to the arterial-based Logan plot (*23*).

A prerequisite for calculation of Logan plot $V_S$ is that a reference region is available, as for the above mentioned ligands (*21, 22*). Here, the cerebellar gray matter was assumed to be devoid of target protein and hence represent only non-specific binding. Although a blocking study would be required to validate the assumption *in vivo* (*24, 25*), strong support comes from various findings. First, no specific AV1451 binding was observed in the cerebellum *post-mortem* across a wide range of clinical populations and methods (*17, 26*). Furthermore, we add *in vivo* data, showing that cerebellar kinetics were equal to those of the cortical areas in healthy controls, all presumably devoid of PHF tau. Nevertheless, average cerebellar $V_T$ obtained from the arterial-based Logan plot was higher in controls than patient groups, which is unlikely to represent specific tau binding as for reasons above. Rather, the increased cerebellar $V_T$ might be attributable to physiological variation and/or potential off-target binding. Usage of $V_T$ as outcome parameter is however not sensitive to detect whether group differences are attributable to changes in $V_S$ or $V_{ND}$. Assuming that $V_{ND}$ is constant across the brain it is informative to account for such differences by deriving $V_S$ or *DVR*. Although various other secondary binding sites have been excluded (*8*), it seems that $^{18}$F-AV1451 binds to some extent to factors present in neuromelanin- and melanin-containing cells (*17*). The potential off-target binding may also be reflected in the higher *in vivo* retention in the basal ganglia (*10, 11, 17, 27*), which was recently linked to iron content (*28*). This was particularly prominent in the healthy control group, with the putamen showing higher SUV and *SUVR* than any other brain region. Further, in AD patients

kinetics of the putamen were markedly different from cortical areas know to be affected by tau aggregates. These findings indicate that $^{18}$F-AV1451 binding in the putamen is not related to PHF, but caused by yet unknown mechanisms potentially involving a secondary binding site. On the other hand, the present results of cortical $^{18}$F-AV1451 binding in AD reflects autoradiography (*17*) and human imaging data (*10*) (supplement).

The results from this work may also have clinical implications. Simplified analyses showed strong agreement of reference region based $BP_{ND}$ and *DVR* as well as *SUVR* when compared to the arterial-based Logan plot. As expected, longer scan times show better agreement, but strong correlations were already observed for 100 min ($R^2 > 0.9$), indicating that reliable results can be obtained with shorter scans. For *SUVR*, the interval 80-100 min seems to provide a robust simplification, which can be realized by a 20 min static scan without blood sampling. This protocol may offer examination of several consecutive patients with a single synthesis followed by simple analysis of calculating ratios. Accordingly, similar differences between AD patients and controls (t-values) for the ratio methods and arterial-based Logan plot were observed. Despite the steady increase of *SUVR* across time in AD patients, the t-values did not increase for longer time intervals, since also the variance in AD increased. Hence, the increase in absolute *SUVR* seems only to affect slope and intercept when compared to the arterial-based Logan plot. Still, a larger patient cohort is required to assess whether the *SUVR* obtained from 80-100 min is sufficient for clinical evaluation, especially as a prognostic marker. Finally, SUV cannot be recommended for clinical evaluation due to high unexplained variance when compared with the arterial-based Logan plot. This was reflected in the underestimated differences between AD patients and controls for various brain regions.

One limitation of this study is the low sample size. However, as the pharmacokinetic characteristics were rather uniform within groups, the data at hand seems to be representative

for a methodological evaluation. Furthermore, we were not aiming to infer statistical differences between groups but rather to identify optimal quantification strategies. The sample size is similar to previous methodological work, which focused on quantitative characterization of novel radioligands (*12, 22, 24*). Another aspect is that no partial volume correction was carried out. Tissue loss may indeed alter the absolute values of the outcome parameters, but since tracer kinetics are not affected, the data seems representative for the evaluation of a quantitative description.

## CONCLUSIONS

The Logan plot is the method of choice for input function-based quantification of $^{18}$F-AV1451 binding. Using cerebellum as reference region, simplified techniques can be employed, potentially offering clinical applicability with a static scan at 80-100 min and ratio methods. Compared to healthy controls, these approaches showed higher *in vivo* binding for AD and to some extent also for CBS patients.

**ACKNOWLEDGEMENTS**

We thank our participating subjects and their families. We are grateful to research nurses Katarina Johansson, Karin Nilsson and Cecilia Dahl; Drs Anna Svenningsson, Alva Månsten and Sofie Mårtensson; PET-technicians Irene Erlandsson, Linda Lim and Eva Nilsson. We thank Drs David Brooks, Per Borghammer and Peter Parbo at Aarhus PET-center, Aarhus University, Denmark for teaching arterial blood sampling.

Work in the authors' laboratory was supported by the European Research Council, the Swedish Research Council, the Strategic Research Area MultiPark (Multidisciplinary Research in Parkinson's disease) at Lund University, the Crafoord Foundation, the Swedish Brain Foundation, the Skåne University Hospital Foundation, the Swedish Alzheimer Association, and the Swedish federal government under the ALF agreement. Funding sources had no role in the design and conduct of the study; in the collection, analysis, interpretation of the data; or in the preparation, review, or approval of the manuscript. The precursor of AV-1451 was generously provided by Avid Radiopharmaceuticals.

**CONFLICT of INTEREST**

The authors report no conflict of interest.

## REFERENCES


**1.** Dani M, Brooks DJ, Edison P. Tau imaging in neurodegenerative diseases. *Eur J Nucl Med Mol Imaging.* 2015:Epub ahead of print.

**2.** Murray ME, Kouri N, Lin WL, Jack CR, Jr., Dickson DW, Vemuri P. Clinicopathologic assessment and imaging of tauopathies in neurodegenerative dementias. *Alzheimers Res Ther.* 2014;6:1.

**3.** Arriagada PV, Growdon JH, Hedley-Whyte ET, Hyman BT. Neurofibrillary tangles but not senile plaques parallel duration and severity of Alzheimer's disease. *Neurology.* 1992;42:631-639.

**4.** Villemagne VL, Fodero-Tavoletti MT, Masters CL, Rowe CC. Tau imaging: early progress and future directions. *Lancet Neurol.* 2015;14:114-124.

**5.** Giacobini E, Gold G. Alzheimer disease therapy--moving from amyloid-beta to tau. *Nat Rev Neurol.* 2013;9:677-686.

**6.** Palmqvist S, Zetterberg H, Mattsson N, et al. Detailed comparison of amyloid PET and CSF biomarkers for identifying early Alzheimer disease. *Neurology.* 2015;85:1240-1249.

**7.** Zimmer ER, Leuzy A, Gauthier S, Rosa-Neto P. Developments in tau PET imaging. *Can J Neurol Sci.* 2014;41:547-553.

**8.** Xia CF, Arteaga J, Chen G, et al. [(18)F]T807, a novel tau positron emission tomography imaging agent for Alzheimer's disease. *Alzheimers Dement.* 2013;9:666-676.

**9.** Chien DT, Bahri S, Szardenings AK, et al. Early clinical PET imaging results with the novel PHF-tau radioligand [F-18]-T807. *J Alzheimers Dis.* 2013;34:457-468.

**10.** Johnson KA, Schultz A, Betensky RA, et al. Tau PET imaging in aging and early Alzheimer's disease. *Ann Neurol.* 2015:Epub ahead of print.

**11.** Shcherbinin S, Schwarz AJ, Joshi AD, et al. Kinetics of the tau PET tracer 18F-AV-1451 (T807) in subjects with normal cognitive function, mild cognitive impairment and Alzheimer's disease. *J Nucl Med.* 2016. Epub ahead of print.

**12.** Gunn RN, Sargent PA, Bench CJ, et al. Tracer kinetic modeling of the 5-HT1A receptor ligand [carbonyl-11C]WAY-100635 for PET. *Neuroimage.* 1998;8:426-440.

**13.** Zanotti-Fregonara P, Hirvonen J, Lyoo CH, et al. Population-based input function modeling for [(18)F]FMPEP-d 2, an inverse agonist radioligand for cannabinoid CB1 receptors: validation in clinical studies. *PloS One.* 2013;8:e60231.

**14.** Wu S, Ogden RT, Mann JJ, Parsey RV. Optimal metabolite curve fitting for kinetic modeling of 11C-WAY-100635. *J Nucl Med.* 2007;48:926-931.

**15.** Logan J, Fowler JS, Volkow ND, et al. Graphical analysis of reversible radioligand binding from time-activity measurements applied to [N-11C-methyl]-(-)-cocaine PET studies in human subjects. *J Cereb Blood Flow Metab.* 1990;10:740-747.

**16.** Innis RB, Cunningham VJ, Delforge J, et al. Consensus nomenclature for in vivo imaging of reversibly binding radioligands. *J Cereb Blood Flow Metab.* 2007;27:1533-1539.

**17.** Marquie M, Normandin MD, Vanderburg CR, et al. Validating novel tau positron emission tomography tracer [F-18]-AV-1451 (T807) on postmortem brain tissue. *Ann Neurol.* 2015;78:787-800.

**18.** Wu Y, Carson RE. Noise reduction in the simplified reference tissue model for neuroreceptor functional imaging. *J Cereb Blood Flow Metab.* 2002;22:1440-1452.

**19.** Logan J, Fowler JS, Volkow ND, Wang GJ, Ding YS, Alexoff DL. Distribution volume ratios without blood sampling from graphical analysis of PET data. *J Cereb Blood Flow Metab.* 1996;16:834-840.

**20.** Declercq L, Celen S, Lecina J, et al. Comparison of new tau PET-tracer candidates with [18F]T808 and [18F]T807. *Mol Imaging.* 2016;15.

**21.** Kimura Y, Ichise M, Ito H, et al. PET Quantification of tau pathology in human brain with 11C-PBB3. *J Nucl Med.* 2015;56:1359-1365.

**22.** Price JC, Klunk WE, Lopresti BJ, et al. Kinetic modeling of amyloid binding in humans using PET imaging and Pittsburgh Compound-B. *J Cereb Blood Flow Metab.* 2005;25:1528-1547.

**23.** Jonasson M, Wall A, Chiotis K, et al. Tracer kinetic analysis of (S)-18F-THK5117 as a PET tracer for assessing tau pathology. *J Nucl Med.* 2016:Epub ahead of print.

**24.** Ginovart N, Meyer JH, Boovariwala A, et al. Positron emission tomography quantification of [11C]-harmine binding to monoamine oxidase-A in the human brain. *J Cereb Blood Flow Metab.* 2006;26:330-344.

**25.** Parsey RV, Kent JM, Oquendo MA, et al. Acute occupancy of brain serotonin transporter by sertraline as measured by [11C]DASB and positron emission tomography. *Biol Psychiatry.* 2006;59:821-828.

**26.** Herrmann M, Golombowski S, Krauchi K, et al. ELISA-quantitation of phosphorylated tau protein in the Alzheimer's disease brain. *European Neurology.* 1999;42:205-210.

**27.** Harada R, Okamura N, Furumoto S, et al. 18F-THK5351: a novel PET radiotracer for imaging neurofibrillary pathology in Alzheimer's disease. *J Nucl Med.* 2015:Epub ahead of print.

**28.** Lowe VJ, Curran G, Fang P, et al. An autoradiographic evaluation of AV-1451 Tau PET in dementia. *Acta Neuropathol Commun.* 2016;4:58.

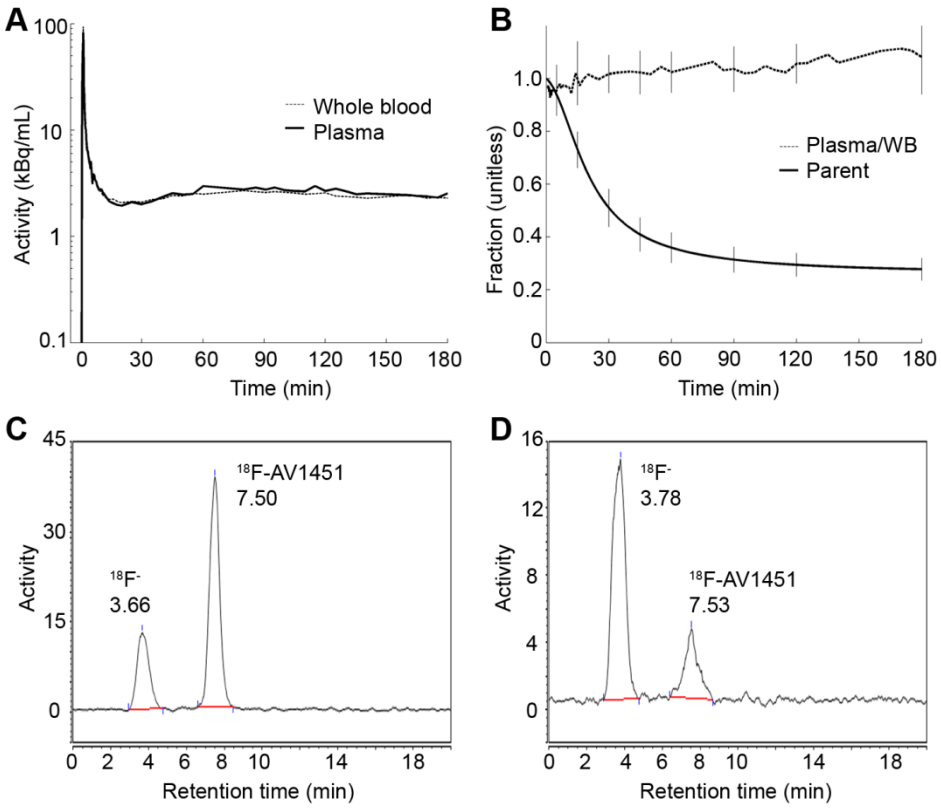


Figure 1: Analysis of blood data. **(A)** Whole blood and plasma activities from a representative healthy subject showing rapid clearance of the radioligand from blood (log scale). **(B)** Parent fraction and plasma-to-whole blood ratio averaged across the entire sample. Bars denote standard deviation. **(C and D)** High performance liquid chromatography profiles obtained from a blood sample 15 min and 120 min post injection. Only one metabolite was observed (presumably $^{18}F^-$) with much shorter retention time (3.7 min) than the parent compound (7.5 min).

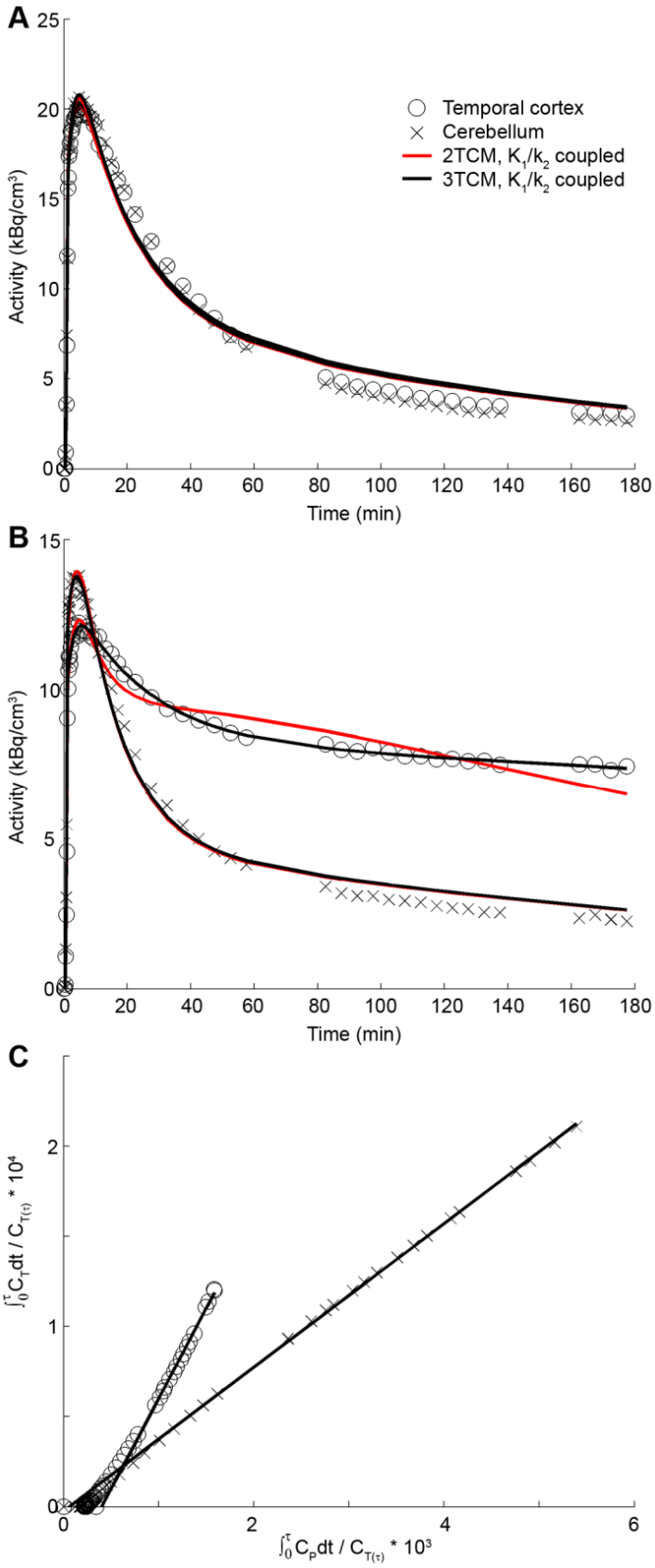


Figure 2: Time activity curves of two subjects and corresponding fits obtained with 2TCM and 3TCM, with $K_1/k_2$ coupled. **(A)** For the healthy control subject cerebellum kinetics were similar to those of the cortex. However, no adequate model fits were obtained with either of the compartment models. **(B)** For the Alzheimer's disease patient the 3TCM gave a marked improvement in the temporal cortex, which was however not obtained for all subjects. Cerebellum TACs showed similar kinetics between the patient and control, but again adequate fits could not be obtained with any of the tissue compartment models. **(C)** Logan plots of the same AD patient showed that linearity was reached fast (at 26.1 ± 17.8min).

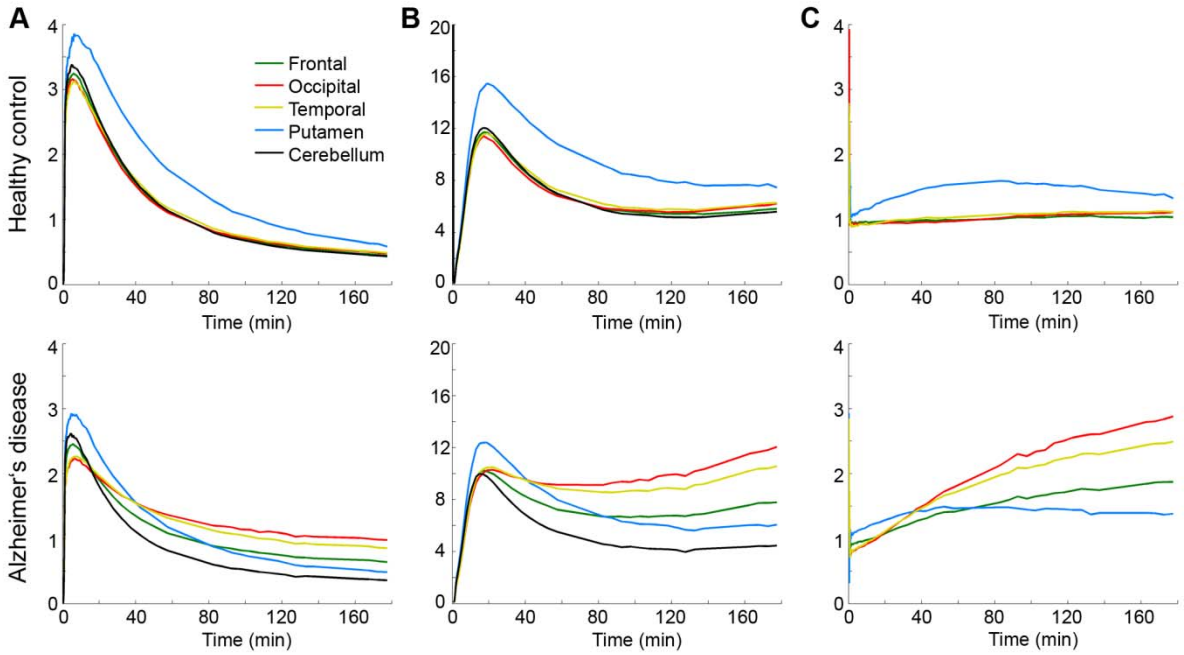


Figure 3: Time activity curves averaged across all subjects for healthy controls and Alzheimer's disease patients for frontal (green), occipital (red) and temporal cortices (yellow), the putamen (blue) and cerebellar gray matter (black). Given are target activities divided by injected dose per kg body weight (SUV) **(A)**, divided by activity in plasma **(B)** and divided by activity in the cerebellum (*SUVR*) **(C)**.

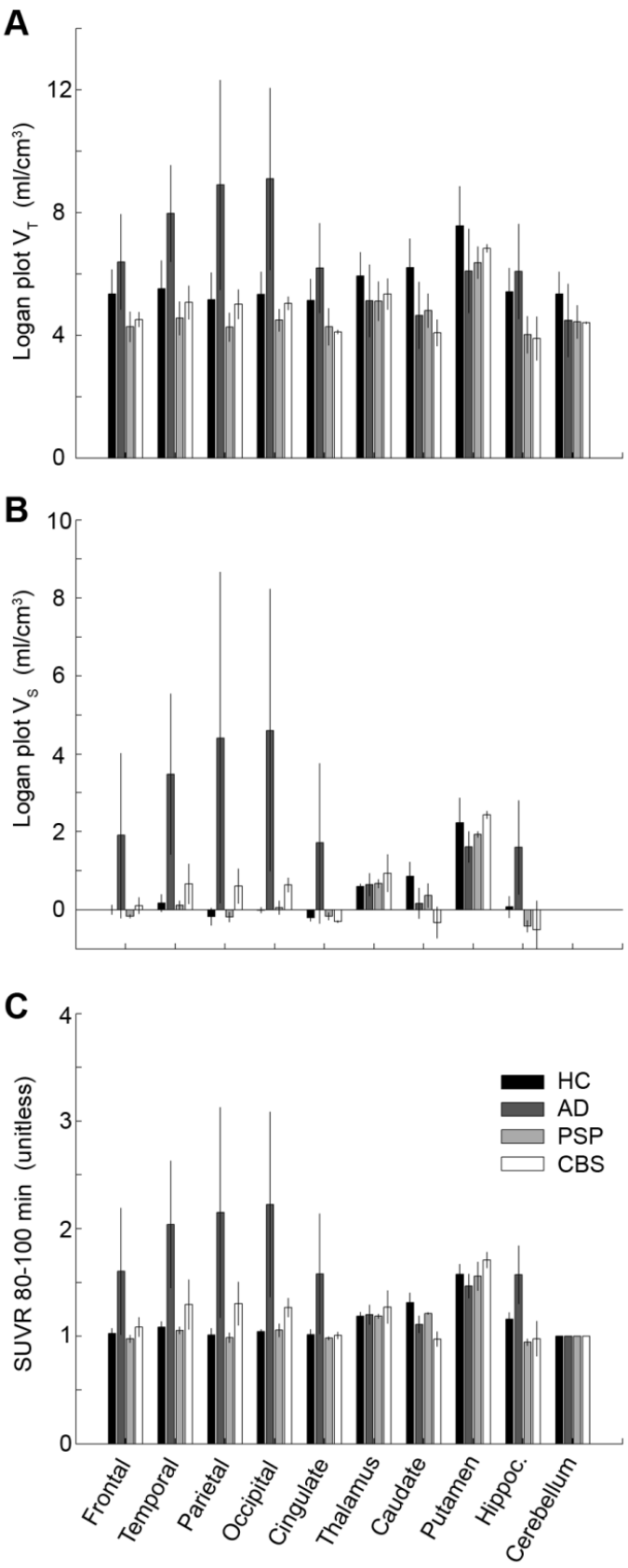


Figure 4: Average $^{18}$F-AV1451 binding for different brain regions and population groups (from dark to bright: HC, AD, PSP, CBS) obtained with the arterial-based Logan plot $V_T$ **(A)**, Logan plot $V_S$ **(B)** and *SUVR* 80-100min **(C)**. AD patients showed higher cortical binding than HC for all outcome parameters. Differences in CBS became only evident for Logan $V_S$ and *SUVR*, hence, after correcting for higher cerebellar $V_T$ in HC. Differences between PSP and HC were generally low.

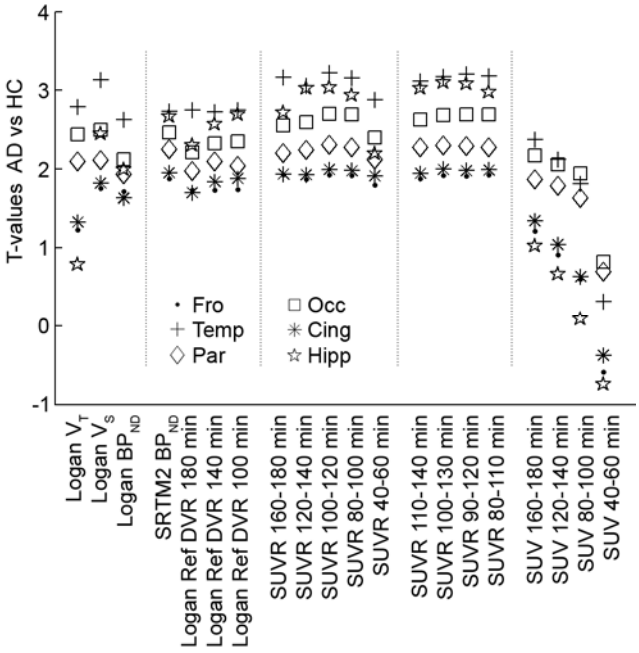


Figure 5: $^{18}$F-AV1451 binding differences between AD patients and controls compared across different quantification methods. T-values were computed since differences in absolute values of various outcome parameters are normalized by their variance. Strongest differences were obtained for arterial-based Logan plot $V_S$ and *SUVR* 100-120 min.

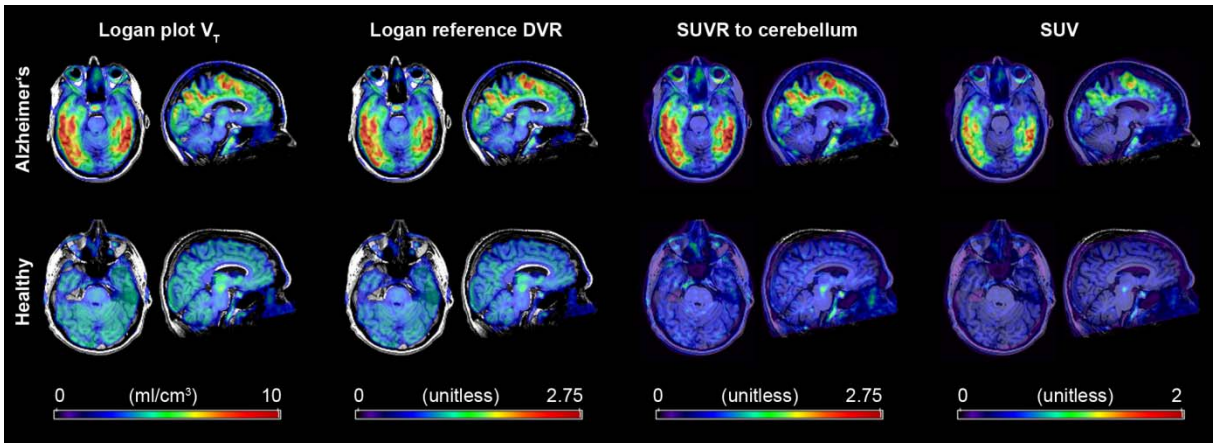


Figure 6: Voxel-wise quantification of $^{18}$F-AV1451 binding in one patient with Alzheimer's disease and one healthy control. Quantification was carried out with the arterial-based ($V_T$, 180min) and reference Logan plots (*DVR*, 100min), ratios between target and cerebellar activities (*SUVR*, 80-100min) and injected dose per kg body weight (SUV, 80-100min). Except for SUV which underestimated the binding, all approaches showed increased binding in the patient in various cortical brain regions.

| | Model | Outcome |
|---|---|---|
| *Arterial-based models* | | |
| 1 | 1TCM | $V_T = K_1/k_2$ |
| 2 | 2TCM ± $K_1/k_2$ coupled | $V_S = K_1*k_3/k_2*k_4$ |
| 3 | 3TCM ± $K_1/k_2$ coupled | $V_S = K_1*k_3/k_2*k_4$ |
| 4 | Logan plot | $V_T$ |
| *Reference region models* | | |
| 5 | SRTM2 ± $k_2$' fixed | $BP_{ND} = k_3/k_4$ |
| 6 | Logan reference plot | $DVR = BP_{ND} + 1$ |
| *Ratio methods* | | |
| 7 | Target/ref | $SUVR = C_T/C_{cerebellum}$ |
| 8 | SUV | SUV = $C_T$/injected dose |

Table 1: Evaluated models and corresponding primary outcome parameter. Reference models used cerebellar gray matter as reference region. Ratio methods were calculated as activity of the target region divided by activity in the reference region (*SUVR* = target/ref) or divided by injected dose per kg body weight (SUV). See table 2 for different time intervals. $BP_{ND}$: binding potential relative to nondisplaceable binding, $C_T$: concentration in target region, *DVR*: distribution volume ratio, SRTM2: simplified reference tissue model 2, TCM: tissue compartment model, $V_T$: total volume of distribution, $V_S$: specific volume of distribution.

| Model | Logan $V_T$ transform | $R^2$ | Slope | Intercept |
|---|---|---|---|---|
| SRTM2 | $(V_T-V_{T\_Cereb})/V_{T\_Cereb}$ | 0.92 | 0.90 | 0.04 |
| SRTM2 $k_2'$ fixed | $(V_T-V_{T\_Cereb})/V_{T\_Cereb}$ | 0.95 | 0.94 | 0.03 |
| **Logan reference 180min** | $\boldsymbol{V_T/V_{T\_Cereb}}$ | **0.99** | **1.06** | **-0.06** |
| Logan reference 140min | $V_T/V_{T\_Cereb}$ | 0.96 | 0.85 | 0.17 |
| Logan reference 100min | $V_T/V_{T\_Cereb}$ | 0.91 | 0.77 | 0.25 |
| Logan reference 60min[a] | $V_T/V_{T\_Cereb}$ | 0.75 | 0.71 | 0.28 |
| Target/ref 160-180min | $V_T/V_{T\_Cereb}$ | 0.94 | 1.34 | -0.29 |
| Target/ref 120-140min | $V_T/V_{T\_Cereb}$ | 0.93 | 1.15 | -0.07 |
| **Target/ref 100-120min** | $\boldsymbol{V_T/V_{T\_Cereb}}$ | **0.94** | **1.02** | **0.07** |
| Target/ref 80-100min | $V_T/V_{T\_Cereb}$ | 0.93 | 0.90 | 0.20 |
| Target/ref 40-60min | $V_T/V_{T\_Cereb}$ | 0.88 | 0.59 | 0.48 |
| Target/ref 110-140min | $V_T/V_{T\_Cereb}$ | 0.93 | 1.12 | -0.04 |
| Target/ref 100-130min | $V_T/V_{T\_Cereb}$ | 0.93 | 1.05 | 0.04 |
| Target/ref 90-120min | $V_T/V_{T\_Cereb}$ | 0.94 | 0.99 | 0.10 |
| Target/ref 80-110min | $V_T/V_{T\_Cereb}$ | 0.93 | 0.92 | 0.17 |
| SUV 160-180min | $V_T$ | 0.82 | 0.13 | -0.18 |
| SUV 120-140min | $V_T$ | 0.82 | 0.13 | -0.10 |
| SUV 80-100min | $V_T$ | 0.79 | 0.13 | 0.04 |
| SUV 40-60min | $V_T$ | 0.69 | 0.13 | 0.46 |

Table 2: Associations of $^{18}$F-AV1451 tau binding between the 180 min arterial-based Logan plot and non-invasive alternatives. Linear regression was carried out between each's model outcome parameter and the correspondingly transformed outcome from the arterial-based Logan plot, e.g., SUVR vs $V_T/V_{T\_Cereb}$. Best agreements are marked bold. [a]: Association was estimated only with n=13 as 2 subjects gave unstable fits for $k_2'$. See table 1 for abbreviations.

**SUPPLEMENTAL MATERIAL**

Modeling strategies for quantification of in vivo $^{18}$F-AV1451 binding in patients with tau pathology

A Hahn, M Schain, M Erlandsson, P Sjölin, GM James, OT Strandberg, D Hägerström, R Lanzenberger, J Jögi, TG Olson, R Smith, O Hansson.

**SUPPLEMENTAL INTRODUCTION**

Several positron emission tomography (PET) radioligands have been developed, which show high sensitivity for tau over amyloid beta (*1, 2*). These include the family of THK-compounds (*3*), $^{11}$C-PBB3 as well as $^{18}$F-T808 and $^{18}$F-AV1451 (formerly known as T807). Of those, only $^{11}$C-PBB3 (*4*) and (S)-$^{18}$F-THK5117 (*5*) have yet undergone full quantitative description. Although robust quantification was obtained both with an arterial-based model and simplified ratio methods, $^{11}$C-PBB3 exhibits a radioactive metabolite that crosses the blood brain barrier, making full quantification challenging. In addition, labeling with carbon-11 may complicate clinical applicability due to the short half-life, which impedes shipping and limits each synthesis to few scans. On the other hand, (S)-$^{18}$F-THK5117 showed promising results, with strong agreement between arterial-based and non-invasive models for PET scans as short as 60min (*5*). However, the radioligand exhibits high white matter uptake and less signal to noise ratio as compared to other THK compounds (*3*). Although $^{18}$F-T808 does not include these issues, the radioligand is subject to substantial defluorination (*6*). The resulting bone uptake may in turn complicate exact quantification of nearby cortical areas due to spill over and partial volume effects occurring from limited PET resolution (*7*).

## SUPPLEMENTAL METHODS

### Subjects

All patients underwent a clinical and neurological exam and were assessed using the Hoehn and Yahr (H&Y) and Schwab and England activities of daily living (S&E) scales as well as several cognitive rating scales, including Mini Mental State Exam (MMSE), A Quick Test of Cognitive Speed (AQT), Symbol Digit Modalities Test (SDMT), Hospital Anxiety and Depression Scale (HADS), Stroop Test and Trail Making Test A (TMT-A). Patients with AD diagnosis met the DSM III-R criteria for dementia and the criteria for probable AD defined by the National Institute of Neurological and Communicative Disorders and Stroke and the Alzheimer's Disease and Related Disorders Association (NINCDS-ADRDA) (*8*). PSP patients were diagnosed according to the National Institute of Neurological Disorders and Stroke (NINDS) criteria (*9*), and were further assessed using the PSP rating scale and the Unified Parkinson's Disease Rating Scale (UPDRS)-III. CBS patients were diagnosed in accordance with clinicopathologic guidelines (*10*). Healthy controls had no previous neurologic or psychiatric disorders. Exclusion criteria were current alcohol or drug abuse, other major or recurrent neurological or psychiatric disorders, inability to undergo magnetic resonance imaging (MRI) and severe renal, hepatic impairment or significant infectious disease.

### Radiolabeling of [18F]AV1451

[$^{18}$F]Fluoride activity was retained on a pre-conditioned Sep-Pak® Light Accell™ Plus (QMA) Cartridge and eluted to the reaction vessel using 0.75 mL of a 0.075 M Tetrabutylammonium Hydrogen Carbonate Solution. The eluted activity was heated at 110 °C under nitrogen flow and vacuum for 5 min and 20 sec while three additions of acetonitrile were made to facilitate the azeotropic removal of water. A solution of AV-1622 [1.5 mg in anhydrous DMSO (1.6 mL)] was added to the reaction vessel and the resulting mixture was kept at 120 °C for 5 min followed by de-protection using 1.0 mL of 2M HCl(aq) at 100 °C for 5 min. After being cooled for 1min, the

crude [$^{18}$F]AV1451 mixture was neutralized with 2.4 mL of 1M NaOH(aq). The resulting mixture was passed through an Oasis® HLB Light cartridge. The retained crude [$^{18}$F]AV1451 was washed with water for injection (WFI) then eluted off the Oasis HLB Light cartridge using 1.5 mL of acetonitrile. The crude [$^{18}$F]AV1451 was diluted with 3.5 mL of WFI/Ethanol (10/1) and loaded onto a semi-preparative Zorbax Eclipse XDB-C18, 9.4 x 250 mm, 5µm HPLC column for purification using the isocratic elution 40 % ethanol /60 % 100 mM phosphate buffer at a 4 mL/min flow rate. The HPLC fraction containing the purified [$^{18}$F]AV1451 was collected (4 mL) and directly transferred into the final vial through a 0.22 µm Cathivex-GS filter. The pH of the solution was adjusted with 2 mL of citrate buffer and the solution was also diluted with 10 mL NaCl 0.9 % to adjust the concentration of ethanol in the final solution.

**Positron emission tomography**

To minimize head motion during the acquisition, the subject's head was strapped to a dedicated head holder. List mode data was acquired from 0-60min, 80-140 min and 160-180 min post injection. For attenuation correction, a separate low dose CT was obtained before each scan session. To reduce motion artifacts, the non-attenuation correction PET images were visually inspected and, if required, manually aligned to the CT image, after which the corresponding sinograms were aligned accordingly. Following this alignment step, the PET images were reconstructed again with attenuation correction, using an iterative Vue Point HD algorithm (6 subsets, 18 iterations, 3 mm filter, no time-of-flight correction). These parameter settings were established using phantom measurements and preliminary data analysis. The acquisitions were reconstructed into frames of 12x10 s, 6x20 s, 6x30 s, 3x60 s, 5x120 s and 8x300 s (0-60 min) as well as 12x300 s (80-140 min) and 4x300 s (160-180 min). The resolution of the PET scanner is 4.7 mm transverse and 4.74 mm axial full-width at half-maximum 1 cm next to the center of the field of view (*11*).

**Blood sampling and determination of radioactive metabolites**

Arterial blood samples were obtained manually every 5 s until 1.5 min post injection, every 10 s until 3 min, every 20 s until 5 min, every 30 s until 8 min, every 1 min until 12 min, every 2 min until 20 min and then every 5 min until the rest of the measurement (excluding PET breaks). Plasma was separated by centrifugation and radioactivity levels in both whole-blood and plasma samples (3 mL each) were measured in a ɣ-counter (PerkinElmer 1480 Wizard).

Determination of radioactive metabolites was carried out for 10 mL samples at 5, 15, 30, 45, 60, 90, 120 and 180 min using high performance liquid chromatography. Plasma was obtained by 6 min centrifugation at 4400 rpm and 4 °C. Plasma proteins were precipitated by adding acetonitrile (2.5 mL) to the plasma (2.5 mL). The resulting mixture was centrifuged at 4400 rpm for 6 min. Two mL of the supernatant was injected into a HPLC to separate the parent tracer from its radioactive metabolites (pump, injector and UV-detector: Ultimate 3000, Dionex; BGO radioactivity detector: Bioscan). The sample was injected on a Chromolith®SemiPrep, RP-18e 100-10 mm column, 100 x 4.6 mm. The tracer and its metabolite were eluted with 0.1 % TFA in H2O and MeCN gradients (0-12 min 15 % to 85 %, 12-16 min 85 %, 16-17 min 85 % to 15 %, 17-20 min 15 %) at a flow rate of 2 mL/min. The eluent from the column was collected in 30 different fractions (1 mL/fraction), each measured in a ɣ-counter to determine the percentage of intact parent compound.

**Magnetic resonance imaging**

Structural images were obtained with a T1-weighted magnetization-prepared rapid gradient echo sequence using a 3T Siemens Skyra scanner (Erlangen, Germany). Sequence parameters were TE/TR = 2.54/1900ms, acquiring 176 slices with 1mm isotropic resolution. Structural images were used for coregistration with PET images and transformation of regions of interest to individual space.

**Data processing**

PET images were corrected for head motion by coregistration of each frame to the first frame within that data set, using a 6 parameter rigid transformation. Delineation of brain regions was carried out automatically as follows. After brain extraction of the structural MR images, the summed PET images of each session were separately coregistered to the MRI. The structural MR image was then spatially normalized to the MNI152 structural template (Montreal Neurological Institute) and segmented into gray and white matter as well as cerebrospinal fluid. Cortical template brain regions (see below for details) were then masked with a 50% gray matter mask in order to reduce spill over from non-gray matter areas, whereas subcortical regions were masked with a tissue mask (consisting of gray and white matter). Using the inverse transformation matrices, the masked brain regions were then warped into PET space, and projected onto the dynamic PET image to obtain regional time activity curves (TACs).

**Regions of interest (ROI)**

The frontal ROI included the frontal pole, the superior, middle and inferior (pars triangularis, pars opercularis) frontal gyrus. The temporal region contained the superior (anterior and posterior divisions), middle and inferior temporal gyrus (anterior, posterior and temporooccipital parts). The parietal ROI included the superior parietal lobe, the supramarginal (anterior and posterior) and the angular gyrus. The occipital region contained lateral occipital (inferior and superior divisions) and the intracalcarine cortices. The cingulate ROI comprised the anterior and posterior cingulate gyrus. If an ROI contained several subparts, TACs were generated from these multiple ROIs as an average weighted by size of the subparts. Regions were averaged for left and right hemisphere, except for CBS patients, where only the affected hemisphere was included.

## SUPPLEMENTAL RESULTS

### Arterial-based models

Compartmental modeling results were similar cortex and hippocampus as well as across the remaining subcortical regions independent of the configuration. The 1TCM did not provide acceptable fits throughout as illustrated by the residuals (Supplemental Fig. 1a) and highest Akaike information criterion values (Supplemental Fig. 2a). For cortical regions, the 2TCM showed poor fits for more than 1 ROI in 8 subjects (Fig. 2a; Supplemental Fig. 1b). Although coupling of $K_1/k_2$ decreased the variance of outcome parameters (Supplemental Fig. 2b), model fits were even worse for 3 subjects (all AD patients, Supplemental Fig. 1c). Adding a third tissue compartment to the model, improved the model fits in these 3 subjects (Fig. 2b) with all other subjects showing identical fits (Supplemental Fig. 1d-e). As expected, parameter variability was poor for the unconstrained 3TCM, whereas coupling $K_1/k_2$ improved this issue.

For subcortical regions, the 2TCM did not reach satisfactory fits in 12 subjects, which did not improve with a 3TCM or when coupling $K_1/k_2$ (Supplemental Fig. 2a). Regarding the cerebellar gray matter, 2TCM fits were not acceptable for 7 subjects. This only improved for 1 subject (AD) when using the 3TCM, but coupling $K_1/k_2$ had no effect.

Using spectral analysis, shortened scan time of 60 or 120 min, weighting data by frame duration (data not shown) or ROI refinement to smaller subregions (Supplemental Fig. 3) did not improve the model fits. As expected, the $V_T$ as outcome parameter showed considerably lower standard errors, however, this does not change the issue of generally poor fits for compartment models.

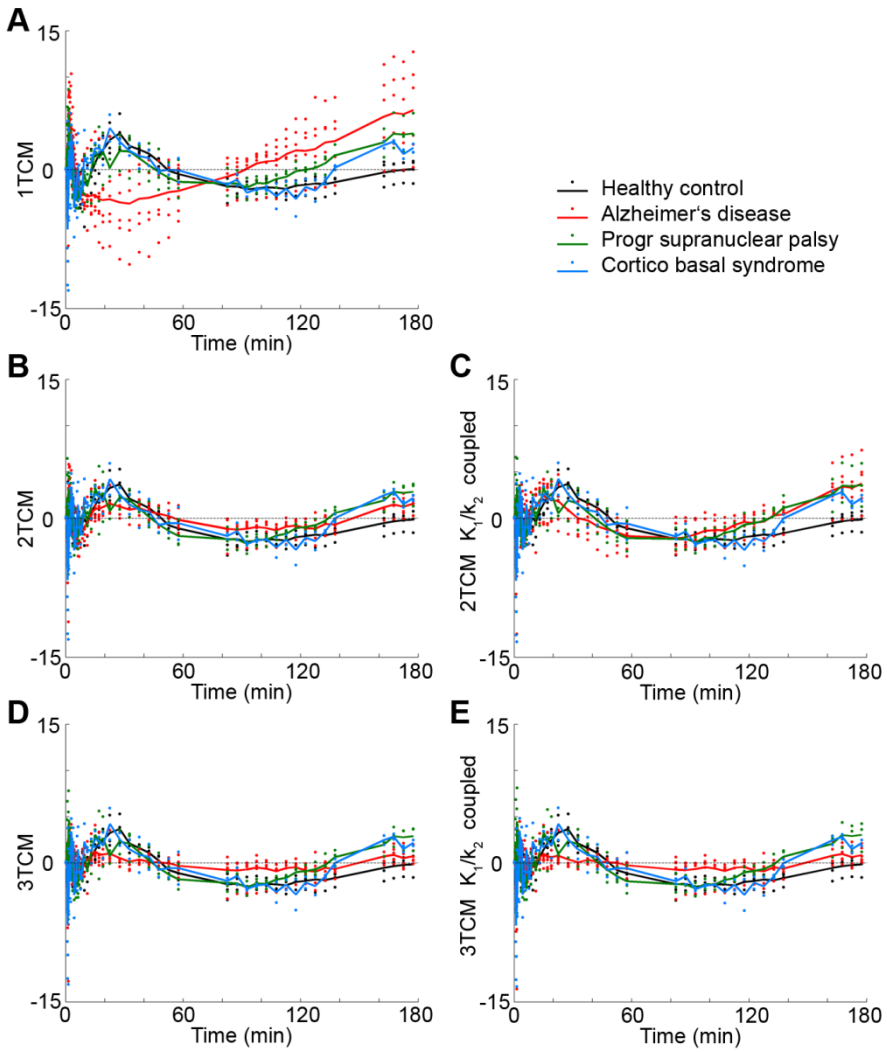


Supplemental figure 1: Weighted residuals obtained from the compartment model fits exemplarily shown for the temporal cortex. Residuals were obviously structured indicating that the models could not describe the data adequately. This was true for all compartment models and population groups except AD patients when using the 3TCM with or without $K_1/k_2$ coupled. Each dot represents one subject, lines represent mean values.

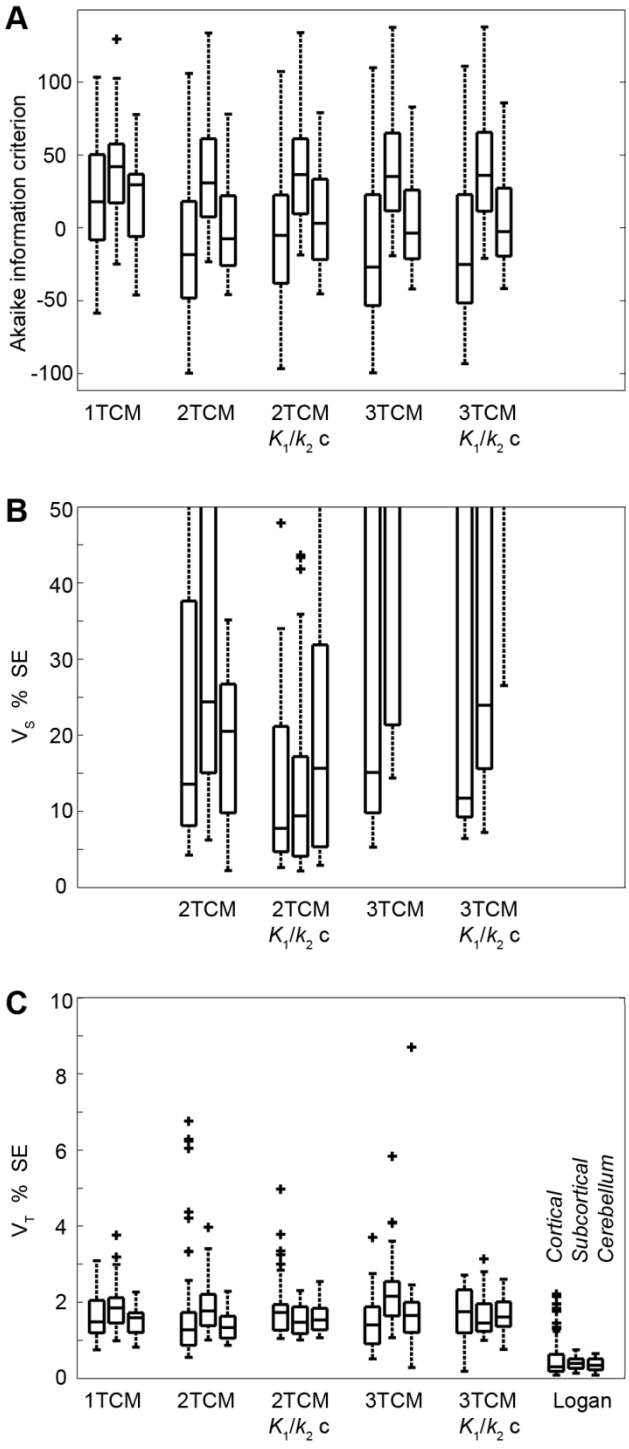


Supplemental figure 2: Modeling results obtained with arterial-based data. Boxplots represent cortical regions plus hippocampus (left), subcortical regions such as thalamus, putamen and caudate (middle) and the cerebellum (right) across all subjects. **(A)** Goodness of fit was determined with the Akaike information criterion for compartment models. Compartment model fits were better for cortex and cerebellum than for subcortical regions but little improvement was obtained with the 3TCM. **(B and C)** Variance of outcome parameters was given by % standard error (SE). Best results were obtained with the 2TCM, $K_1/k_2$ coupled for $V_S$ **(B)** and with the Logan plot for $V_T$ **(C)**.

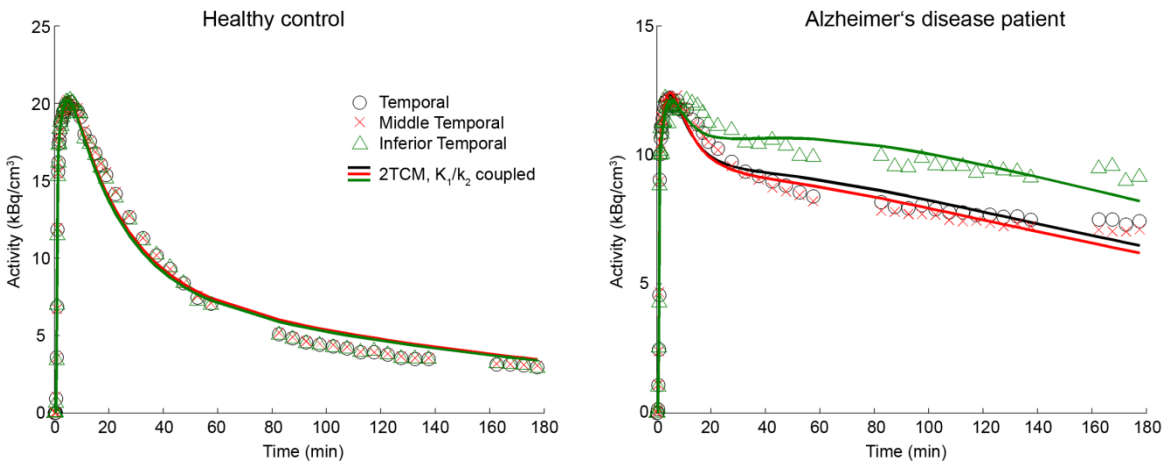


Supplemental figure 3: Time activity curves and corresponding model fits obtained with the 2TCM, $K_1/k_2$ coupled for subregions of the temporal cortex with presumably high and homogenous radioligand uptake (same subjects as in figure 3). **(A)** For the healthy control subject, subregions did not show a relevant difference. **(B)** For the Alzheimer's disease patient the uptake was indeed highest in the inferior temporal cortex, which may be relevant for clinical applications. However, ROI refinement did not improve the model fits.

## SUPPLEMENTAL DISCUSSION

We observed slightly increased cortical binding in CBS but not PSP patients. This fits with post-mortem data as both groups exhibit the straight filament (*12, 13*) and AV1451 binds only to a lesser extent to this isoform (*14*). The remaining *in vivo* difference observed here may thus be related to other characteristics, such as binding to astrocytic plaques (CBS) and tufted astrocytes (PSP) (*12, 13*) as well as no (PSP), intermediate (CBS) and strong binding to N-terminal tau parts (AD) (*15*). On the other hand, the present results of $^{18}$F-AV1451 binding in AD reflects autoradiography (*14*) and human imaging data (*16*), where higher binding in parietal and occipital cortices is presumably attributable to PHF containing neurites in addition to PHF tangles (*14, 17*). Notably, (S)-$^{18}$F-THK5117 showed a rather different topology with highest binding in the amygdala, temporal and frontal regions (*5*), indicating that this compound may only bind to PHF tangles but not PHF containing neurites. The potential consequences of the regionally different binding between the ligands with respect to diagnosis and outcome still remain to be evaluated.

## SUPPLEMENTAL REFERENCES


**1.** Dani M, Brooks DJ, Edison P. Tau imaging in neurodegenerative diseases. *Eur J Nucl Med Mol Imaging.* 2015:Epub ahead of print.

**2.** Zimmer ER, Leuzy A, Gauthier S, Rosa-Neto P. Developments in tau PET imaging. *Can J Neurol Sci.* 2014;41:547-553.

**3.** Harada R, Okamura N, Furumoto S, et al. 18F-THK5351: a novel PET radiotracer for imaging neurofibrillary pathology in Alzheimer's disease. *J Nucl Med.* 2015:Epub ahead of print.

**4.** Kimura Y, Ichise M, Ito H, et al. PET quantification of tau pathology in human brain with 11C-PBB3. *J Nucl Med.* 2015;56:1359-1365.

**5.** Jonasson M, Wall A, Chiotis K, et al. Tracer kinetic analysis of (S)-18F-THK5117 as a PET tracer for assessing tau pathology. *J Nucl Med.* 2016:Epub ahead of print.

**6.** Chien DT, Szardenings AK, Bahri S, et al. Early clinical PET imaging results with the novel PHF-tau radioligand [F18]-T808. *J Alzheimers Dis.* 2014;38:171-184.

**7.** Pike VW. PET radiotracers: crossing the blood-brain barrier and surviving metabolism. *Trends Pharmacol Sci.* 2009;30:431-440.

**8.** McKhann G, Drachman D, Folstein M, Katzman R, Price D, Stadlan EM. Clinical diagnosis of Alzheimer's disease: report of the NINCDS-ADRDA Work Group under the auspices of Department of Health and Human Services Task Force on Alzheimer's Disease. *Neurology.* 1984;34:939-944.

**9.** Litvan I, Agid Y, Calne D, et al. Clinical research criteria for the diagnosis of progressive supranuclear palsy (Steele-Richardson-Olszewski syndrome): report of the NINDS-SPSP international workshop. *Neurology.* 1996;47:1-9.

**10.** Litvan I, Hauw JJ, Bartko JJ, et al. Validity and reliability of the preliminary NINDS neuropathologic criteria for progressive supranuclear palsy and related disorders. *J Neuropathol Exp Neurol.* 1996;55:97-105.

**11.** Bettinardi V, Presotto L, Rapisarda E, Picchio M, Gianolli L, Gilardi MC. Physical performance of the new hybrid PETCT Discovery-690. *Med Phys.* 2011;38:5394-5411.

**12.** Murray ME, Kouri N, Lin WL, Jack CR, Jr., Dickson DW, Vemuri P. Clinicopathologic assessment and imaging of tauopathies in neurodegenerative dementias. *Alzheimers Res Ther.* 2014;6:1.

**13.** Tolnay M, Probst A. The neuropathological spectrum of neurodegenerative tauopathies. *IUBMB Life.* 2003;55:299-305.

**14.** Marquie M, Normandin MD, Vanderburg CR, et al. Validating novel tau positron emission tomography tracer [F-18]-AV-1451 (T807) on postmortem brain tissue. *Ann Neurol.* 2015;78:787-800.

**15.** Ferrer I, Lopez-Gonzalez I, Carmona M, et al. Glial and neuronal tau pathology in tauopathies: characterization of disease-specific phenotypes and tau pathology progression. *J Neuropathol Exp Neurol.* 2014;73:81-97.

**16.** Johnson KA, Schultz A, Betensky RA, et al. Tau PET imaging in aging and early Alzheimer's disease. *Ann Neurol.* 2015:Epub ahead of print.

**17.** Arnold SE, Hyman BT, Flory J, Damasio AR, Van Hoesen GW. The topographical and neuroanatomical distribution of neurofibrillary tangles and neuritic plaques in the cerebral cortex of patients with Alzheimer's disease. *Cereb Cortex.* 1991;1:103-116.